AMPK activation protects against diet-induced obesity through Ucp1-independent thermogenesis in subcutaneous white adipose tissue

Alice E. Pollard^{1,2}, Luís Martins¹, Phillip J. Muckett¹, Sanjay Khadayate¹, Aurélie Bornot², Maryam Clausen³, Therese Admyre³, Mikael Bjursell³, Rebeca Fiadeiro¹, Laura Wilson¹, Chad Whilding¹, Vassilios N. Kotiadis⁴, Michael R. Duchen⁶, Daniel Sutton⁵, Lucy Penfold¹, Alessandro Sardini¹, Mohammad Bohlooly-Y³, David M. Smith², Jon A. Read², Michael A. Snowden², Angela Woods^{1*} and David Carling⁶,6*

Obesity results from a chronic imbalance between energy intake and energy output but remains difficult to prevent or treat in humans. Adenosine monophosphate (AMP)-activated protein kinase (AMPK) is an important regulator of energy homeostasis1-3 and is a molecular target of drugs used for the treatment of metabolic diseases, including obesity^{4,5}. Here we show that mice expressing a gain-of-function AMPK mutant⁶ display a change in morphology of subcutaneous white adipocytes that is reminiscent of browning. However, despite a dramatic increase in mitochondrial content, Ucp1 expression is undetectable in these adipocytes. In response to a high-fat diet (HFD), expression of skeletal muscle-associated genes is induced in subcutaneous white adipocytes from the gain-offunction AMPK mutant mice. Chronic genetic AMPK activation results in protection against diet-induced obesity due to an increase in whole-body energy expenditure, most probably because of a substantial increase in the oxygen consumption rate of white adipose tissue. These results suggest that AMPK activation enriches, or leads to the emergence of, a population of subcutaneous white adipocytes that produce heat via Ucp1-independent uncoupling of adenosine triphosphate (ATP) production on a HFD. Our findings indicate that AMPK activation specifically in adipose tissue may have therapeutic potential for the treatment of obesity.

We previously reported a mouse model expressing a gain-of-function mutation in the $\gamma 1$ subunit of AMPK (mutation of aspartate residue 316 to alanine in mouse Prkag1; D316A) and showed that liver-specific activation of AMPK prevents steatosis on a high-fructose diet⁶. However, AMPK activation in the liver has no detectable metabolic effects in mice fed either a standard chow diet or a HFD⁶. To determine the effect of more widespread AMPK activation, we crossed mice harboring the gain-of-function AMPK $\gamma 1$ transgene with mice expressing Cre-recombinase under the control of the β -actin promoter (β -actin-Cre), generating D316A-Tg mice. As a control, mice harboring wild-type $\gamma 1$ were crossed with β -actin-cre (hereafter referred to as WT-Tg).

Both WT-Tg and D316A-Tg mice were viable, and transgene expression in a range of tissues was confirmed by blotting with an anti-Flag antibody (a Flag epitope was engineered at the C terminus of the transgene; Supplementary Fig. 1a). In humans, gain-of-function mutations in AMPKy2 lead to a cluster of severe cardiac abnormalities, including cardiac hypertrophy and ventricular pre-excitation (Wolff-Parkinson-White syndrome), as well as bradycardia¹. There was a modest increase in heart weight but no change in PR interval, QRS complex duration or heart rate in D316A-Tg mice compared with WT-Tg mice (Supplementary Table 1). Previous studies have indicated a role for AMPK in the regulation of feeding^{7,8}, but there was no significant difference in body weight or food intake between WT-Tg and D316A-Tg mice maintained on a standard chow diet (Supplementary Fig. 1b,c). Similarly, no significant differences in oxygen consumption or body temperature were detected on a chow diet (Supplementary Fig. 1d,e). Strikingly, however, on a HFD, D316A-Tg mice gained much less weight than WT-Tg mice (Fig. 1a and Supplementary Fig. 2a). The reduction in body weight was accounted for by a decrease in fat mass but not lean mass (Fig. 1b). Liver, subcutaneous white adipose tissue (WATsc) and brown adipose tissue (BAT) weights were all significantly reduced in D316A-Tg mice, whereas gonadal WAT weight was not reduced (Fig. 1c). Similar effects were seen in female mice (Supplementary Fig. 2b-d). Lipid accumulation in the liver was also significantly lower in D316A-Tg than WT-Tg mice (Fig. 1d). There was no significant difference in glucose tolerance (Fig. 1e), but fasted plasma insulin levels were significantly lower in D316A-Tg mice (Fig. 1f), thus leading to a significant improvement in insulin sensitivity, as determined by the Homeostatic Model Assessment of Insulin Resistance (Fig. 1g). Food intake was not significantly different on the HFD (Fig. 1h), but oxygen consumption in D316A-Tg mice was significantly greater than that in WT-Tg mice (Fig. 1i,j) without any significant change in movement (Supplementary Fig. 2e). Increased oxygen consumption was still evident when calculated on a permouse basis (Supplementary Fig. 2f). The respiratory exchange ratio was significantly increased in D316A-Tg mice (Fig. 1k,l).

¹MRC London Institute of Medical Sciences, Imperial College London, Hammersmith Hospital, London, UK. ²Discovery Sciences IMED Biotech Unit, AstraZeneca, Cambridge, UK. ³Discovery Sciences IMED Biotech Unit, AstraZeneca, Gothenburg, Sweden. ⁴Department of Cell and Developmental Biology and UCL Consortium for Mitochondrial Research, University College London, London, UK. ⁵Drug Safety and Metabolism IMED Biotech Unit, AstraZeneca, Babraham, UK. ⁶Institute of Clinical Sciences, Imperial College London, Hammersmith Hospital, London, UK.

^{*}e-mail: angela.woods@lms.mrc.ac.uk; david.carling@lms.mrc.ac.uk

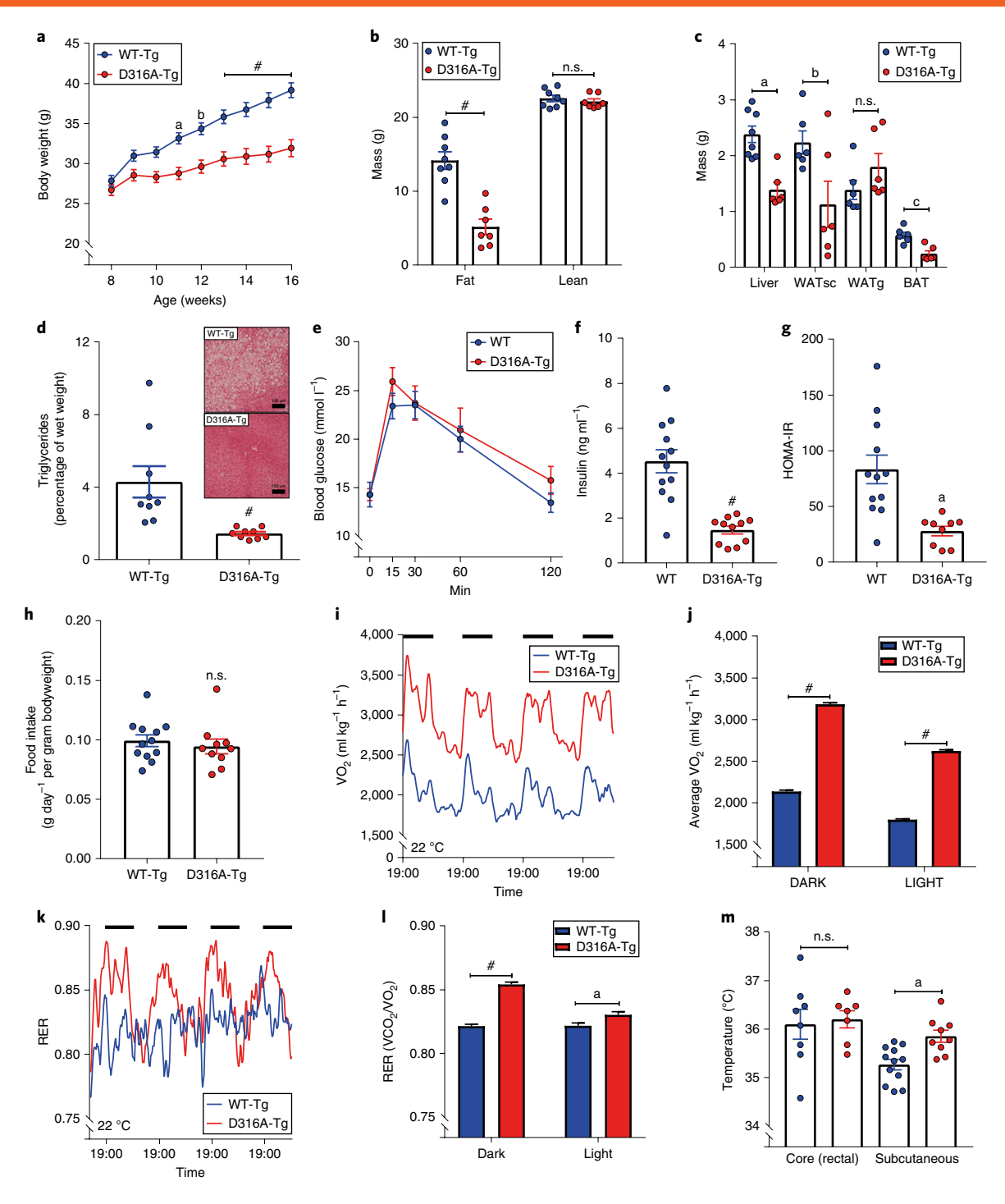


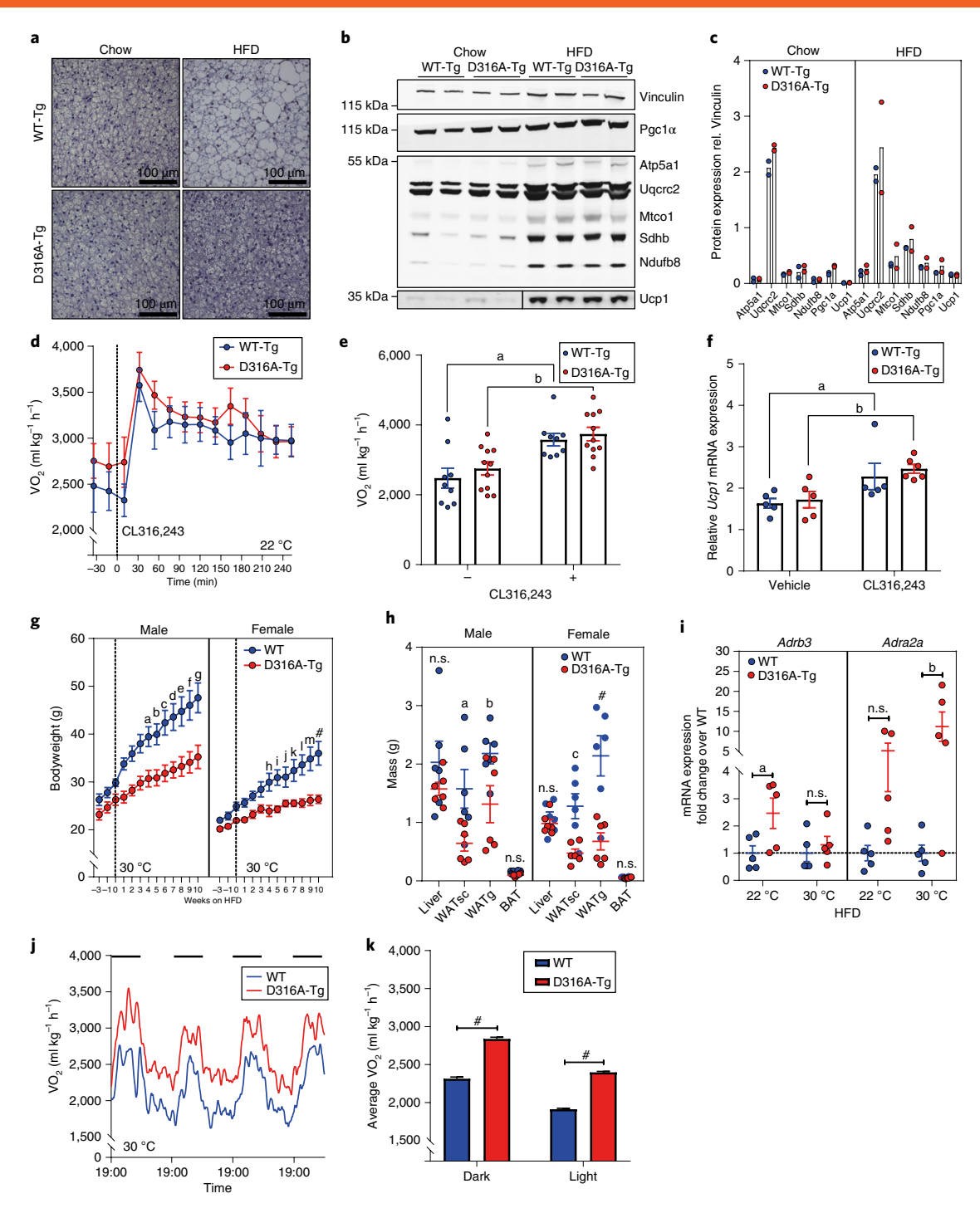
Fig. 1| AMPK activation protects against diet-induced obesity by increasing energy expenditure. a, Male mice expressing either wild-type γ 1 (WT-Tg) or the D316A γ 1 transgene (D316A-Tg) were fed a HFD from 8 weeks of age. Body weight (n=20 for WT-Tg and 17 for D316A-Tg). ^{n}P =0.002, ^{n}P =0.0006 and $^{#}P$ <0.0001. b, Total body fat and lean mass after 8 weeks on a HFD ($^{#}P$ <0.0001). c, Tissue weights after 16 weeks on a HFD (n=8 per genotype; ^{n}P =0.0004, ^{n}P =0.0378, ^{n}P =0.0012, n.s., not significant). d, Liver triglyceride levels in mice fed a HFD for 16 weeks (n=9 per genotype; ^{n}P <0.0001). A representative image (from nine independent mice per genotype) of haematoxylin- and eosin-stained liver sections from HFD-fed mice is shown as an inset. e, Oral glucose tolerance test and f, fasted (6 h) serum insulin levels of mice fed a HFD for 12 weeks (n=12 for WT-Tg and 11 for D316A-Tg; ^{n}P <0.0001). g, Homeostatic Model Assessment of Insulin Resistance (HOMA-IR) calculated from 6h-fasted glucose and insulin levels (n=12 for WT-Tg and 9 for D316A-Tg, ^{n}P =0.0012). h, Food intake over a 5-d period (n=12 for WT-Tg and 10 for D316A-Tg, n.s., not significant). i, Whole-body oxygen consumption (VO₂) monitored continuously over an 84-h period. j, Average VO₂ during 12-h light/12-h dark periods (latter represented by solid black bars). Data points from individual mice were omitted from the graph to show mean values and error-bar sizes more clearly. ^{n}P <0.0001. i-I, mice were fed a HFD for 6 weeks (n=8 for WT-Tg and 6 for D316A-Tg). m, Core (n=8 for WT-Tg and 7 for D316A-Tg) and subcutaneous (n=12 for WT-Tg and 9 for D316A-Tg) body temperatures in mice fed a HFD for 12 weeks. ^{n}P =0.0022, n.s., not significant). In all cases, the results shown are the mean ± s.e.m. Statistical analyses in a,b,e,j,I were performed with two-way analysis of variance (ANOVA) followed by Bonferroni's multiple-comparisons test. Statistical analyses in a,b,e,j,I were performed with tw

Interestingly, although core body temperature was not altered, the surface temperature of D316A-Tg mice was significantly raised (Fig. 1m), a finding indicative of increased energy expenditure.

The findings described above suggest that the primary mechanism for decreased weight gain and fat accumulation in the D316A-Tg mice was mediated by an increase in diet-induced thermogenesis, thus resulting in increased energy expenditure on a HFD. In mammals, BAT plays an important role in thermogenesis, contributing to increased energy expenditure. Numerous studies have revealed that proton leakage across the inner mitochondrial membrane, mediated by the action of uncoupling protein 1 (Ucp1), generates heat rather than ATP production in BAT9,10. On a chow diet, there was no difference in BAT weight between WT-Tg and D316A-Tg mice, and histological analysis revealed no obvious difference in BAT morphology. On a HFD, adipocytes from BAT of D316A-Tg mice were smaller, and contained smaller lipid droplets, than cells isolated from WT-Tg mice (Fig. 2a). The transcriptional co-activator Pgc1α is a key regulator of BAT function and is upregulated in response to cold exposure, coordinating a number of changes including increased mitochondrial biogenesis. There were no differences in expression of Pgc1α or components of the mitochondrial electron-transport chain between the two mouse lines in BAT, although there was increased expression of Pgc1α and mitochondrial proteins, including Ucp1, following feeding of a HFD (Fig. 2b,c), as reported previously^{11,12} To probe BAT function directly, we used the β3-adrenoreceptor (β3-AR) agonist CL316,243. Both WT-Tg and D316A-Tg mice showed a similar increase in oxygen consumption in response to acute treatment with CL316,243 (Fig. 2d,e), as well as a similar increase in messenger RNA expression for Ucp1 (Fig. 2f). These results suggest that AMPK activation does not have a significant effect on BAT function in vivo, and that BAT-mediated thermogenesis does not play a major role in the protection against diet-induced obesity observed in our model. To confirm this, we housed mice at 30 °C, which is within the thermoneutral zone for mice, in which there is no requirement for thermogenesis to maintain body temperature¹³. Under thermoneutral conditions, both male and female mice expressing D316A-Tg were protected against HFD-induced obesity (Fig. 2g), with significant reductions in white adipose tissue mass (Fig. 2h). As anticipated, expression of Adrb3 (encoding β3-AR) was significantly reduced in BAT from mice housed at 30 °C relative to 22 °C (Supplementary Fig. 2g). In WAT there was a modest increase in expression of Adrb3 in D316A-Tg relative to WT-Tg mice housed at 22 °C, but this effect was ablated at 30 °C (Fig. 2i). In contrast, expression of Adra2a (encoding α2a-AR) was significantly increased in D316A-Tg mice compared to WT-Tg at 30°C (Fig. 2i). Oxygen consumption in D316A-Tg mice maintained at 30 °C was significantly greater than that in WT-Tg mice (Fig. 2j,k). These results support the hypothesis that AMPK activation protects against diet-induced obesity through increased energy expenditure mediated by BAT-independent mechanisms.

In contrast to those in BAT, most adipocytes in WAT do not express Ucp1. Adaptation to cold exposure significantly increases the number of cells expressing Ucp1, a process that has been termed 'browning'. These beige, or 'brite' (brown-like in white), adipocytes have a similar overall morphology to that of brown adipocytes, including greater numbers of mitochondria and multilocular fat droplets^{14,15}, and express genes (including Ucp1) that are usually associated with brown adipocytes¹⁶. We observed dramatic changes in the morphology of WATsc (Fig. 3a), but not of gonadal WAT (Supplementary Fig. 3a), between WT-Tg and D316A-Tg mice maintained on either a chow diet or HFD. There was a striking increase in the number of cells containing multilocular lipid droplets in D316A-Tg mice on both chow and HFD. Quantification revealed a marked shift towards smaller lipid droplets in adipocytes from D316A-Tg mice (Fig. 3b-d). We measured oxygen consumption rate (OCR) in WATsc explants and found that there was a significant increase in basal OCR, as well as an increase in spare respiratory capacity, in tissue explants from D316A-Tg mice (Fig. 3e). Importantly, these changes were maintained in explants isolated from D316A-Tg mice housed at 30 °C (Fig. 3f). In agreement with increased OCR, there was a marked increase in mitochondrial content in WATsc isolated from D316A-Tg mice on both chow and HFD, as determined by immunofluorescence using an antibody against Tom-20, a mitochondrial outer-membrane protein (Fig. 3g). Similarly to classical browning, this effect was spread throughout the WATsc depot but showed a heterogeneous distribution. On a HFD, there was a marked increase in Pgc1α protein expression, together with increased expression of components of the mitochondrial electron-transport chain (Fig. 3h,i). More modest changes in protein expression of Pgc1α and electron-transport-chain proteins were also seen in mice maintained on a chow diet (Supplementary Fig. 3b,c). These changes are consistent with the process of browning typically seen in WAT in response to cold adaptation¹⁷. Importantly, however, there was no difference in Ucp1 mRNA expression in WATsc from D316A-Tg mice versus WT-Tg fed a HFD (Fig. 3j), and Ucp1 protein was not detectable (Fig. 3k). Although the role of Ucp1 is generally accepted as being essential for dissipation of the mitochondrial proton gradient and thermogenesis in brown fat, the existence of Ucp1-independent mechanisms that contribute to heat generation in beige adipocytes has been reported¹⁸⁻²⁰. The results of the current study are consistent with a Ucp1-independent phenomenon. Crucially, in our current study, we observed increased thermogenesis in response to high-fat feeding, rather than cold adaptation or β3-adrenergic stimulation as reported previously.

To further investigate the mechanism underlying the Ucp1independent thermogenesis in the D316A-Tg model, we performed a global transcriptomic analysis from WATsc isolated from mice fed a HFD. An obvious feature that emerged was the marked increase in expression of skeletal muscle-selective genes in tissue from D316A-Tg mice (Fig. 4a-c). Of the 100 most differentially expressed genes, 71 were identified as being associated with skeletal muscle function and/or development. Notably, genes encoding proteins involved in Ucp1-independent thermogenic pathways were included in these most highly upregulated transcripts. Ckmt2, which encodes the sarcomeric form of mitochondrial creatine kinase, was recently identified as an important component of a creatine-dependent ADP/ATP substrate cycling mechanism that is activated in inguinal beige adipocytes in response to cold exposure²⁰. On a HFD, Ckmt2 mRNA was increased over 30-fold in WATsc from D316A-Tg mice compared to WT-Tg and, in agreement with this finding, Ckmt2 protein was also significantly increased (Fig. 4d,e). In a previous study²⁰, β-guanidinopropionic acid, a creatine analogue that inhibits creatine transport²¹, was shown to antagonize creatine-driven thermogenesis. However, we were unable to detect any significant effect of β -guanidinopropionic acid on body weight or WATsc mass (Supplementary Fig. 4) in either WT-Tg or D316A-Tg mice fed a HFD. These results suggest that creatine futile cycling is not essential for the effects on energy expenditure seen in our model. Studies in fish have revealed that a specialized type of muscle, called heater organs, has evolved that uses Ca2+ transport to produce heat without muscle contraction²². In this mechanism, a naturally leaky ryanodine receptor increases cytosolic Ca²⁺, activating Ca2+ transport via Ca2+-ATPases. Some of the energy released from ATP hydrolysis by Ca²⁺-ATPase is released in the form of heat²³. Two of the key components required for Ca²⁺ cycling-mediated thermogenesis, sarcoplasmic/endoplasmic reticulum Ca²⁺-ATPase 1 (Sercal; encoded by Atp2a1) and ryanodine receptor 1 (Ryr1), were also significantly upregulated in D316A-Tg mice (Fig. 4b), and immunoblotting revealed a significant increase in Sercal protein expression (Fig. 4d,e). A recent study has reported that Serca2b and Ryr2 are involved in Ca2+-cycling-dependent thermogenesis in beige adipose tissue in response to β3-AR stimulation²⁴.



Interestingly, neither *Atp2a2* (encoding Serca2) nor *Ryr2* mRNA expression was increased in our model (Fig. 4a), and Serca2 protein expression was not detected in WATsc (Fig. 4d). These findings suggest that different signalling pathways might lead to isoform-selective Ca²⁺ cycling in WAT. Further studies are required to elucidate whether the thermogenic response stimulated by the combined effect of HFD feeding and AMPK activation utilizes a Ca²⁺ cycling mechanism involving Serca1 and Ryr1, analogous to the mechanism reported in beige adipose tissue²⁴. It is possible that multiple mechanisms—for example, creatine cycling and Ca²⁺cycling—may contribute to the thermogenic phenotype and/or that other novel mechanisms are involved.

In contrast to the changes in gene expression observed on a HFD, transcriptomic analysis of WATsc from mice fed a chow diet revealed a strikingly different pattern of expression. More than 3,000 genes were significantly changed (fold change > 1.5, P < 0.05) between WT-Tg and D316A-Tg mice (Fig. 4f). Genes in pathways involved in fatty acid metabolism, the tricarboxylic acid (TCA) cycle, mitochondrial ATP production and glycolysis were all highly enriched in WATsc from D316A-Tg mice (Fig. 4g,h), whereas skeletal muscle—associated genes, including Atp2a1 and Ryr1, were downregulated (Fig. 4f). Together, these results show that on a HFD, but not on a chow diet, AMPK activation induces a switch in WATsc towards a skeletal muscle—like phenotype. In contrast, on a chow diet, AMPK activation leads to changes in expression of genes involved in catabolic pathways, including glycolysis and the TCA cycle.

Our findings suggest that activation of AMPK increases the proportion of brown-like adipocytes within the WATsc depot but that these cells differ from conventional beige adipocytes, because they do not express Ucp1. Switching mice from a chow to a HFD resulted in a marked change in transcriptional response in these brown-like cells, thus leading to increased expression of skeletal muscle-associated genes. We propose that these adipocytes, referred to as skeletal muscle-like AMPK reprogrammed thermogenic (SMART) adipocytes, might represent a previously unrecognized cell type or a phenotype that ordinary subcutaneous white adipocytes can attain during sustained AMPK activation. Elegant studies using lineagetracing techniques have revealed that different types of adipocytes can develop from the same pool of progenitor cells that give rise to skeletal muscle cells^{16,25,26}. Current evidence suggests that myocytes and brown adipocytes arise from a Myf5+ precursor, whereas white adipocytes are descended from a different precursor. Most studies indicate that beige adipocytes derive from a white adipocyte precursor (Myf5⁻) stemming mainly from the WATsc depot, and that their development is increased in response to cold adaptation^{16,25,26}.

To further study the origin of these SMART adipocytes, we crossed $\gamma 1$ transgenic mice with mice expressing Cre-recombinase under the control of the adiponectin promoter (Adipoq-Cre),

which drives expression in mature white and brown adipocytes²⁷ but not in adipocyte precursor cells²⁸, to generate WT-Tg^{Adipoq-Cre} and D316A-Tg^{Adipoq-Cre} mice. In contrast to the results obtained from D316A-Tg mice crossed with β-actin-Cre, there was no change in body weight, fat mass or liver WATsc or BAT histology between the two genotypes on a HFD (Supplementary Fig. 5). These results demonstrate that AMPK activation in mature white or brown adipocytes is not sufficient to recapitulate the metabolic phenotype observed in the β-actin-Cre line. This suggests that AMPK activation in a different population of white adipocytes is responsible for the metabolic phenotype, thus distinguishing this model from many previous models showing changes in thermogenesis mediated by expression in mature adipocytes. Next, we crossed the γ1 transgenic lines with mice expressing Cre-recombinase under the control of the platelet-derived growth factor receptor (Pdgfr) α -promoter, to generate WT-Tg^{Pdgfrα-Cre} and D316A-Tg^{Pdgfrα-Cre} mice. Previous studies have shown that this Cre-line drives expression in most adipocyte precursors present in WAT^{28,29}. Similarly to the results with Adipoq-Cre, there were no significant phenotypic changes between genotypes (Supplementary Fig. 5). This finding indicates that the precursor cell leading to the newly defined SMART adipocytes is distinct from Pdgfrα-expressing pre-adipocytes. Although unlikely, it remains possible that activation of AMPK in skeletal muscle could drive the phenotype seen in the global mouse model. We therefore crossed the $\gamma 1$ transgenic lines with mice expressing Cre-recombinase under the control of the Mef2c promoter to drive expression in skeletal muscle. Again, there were no significant phenotypic changes between genotypes on a HFD (Supplementary Fig. 5), thus ruling out skeletal muscle as the primary tissue driving protection against diet-induced obesity.

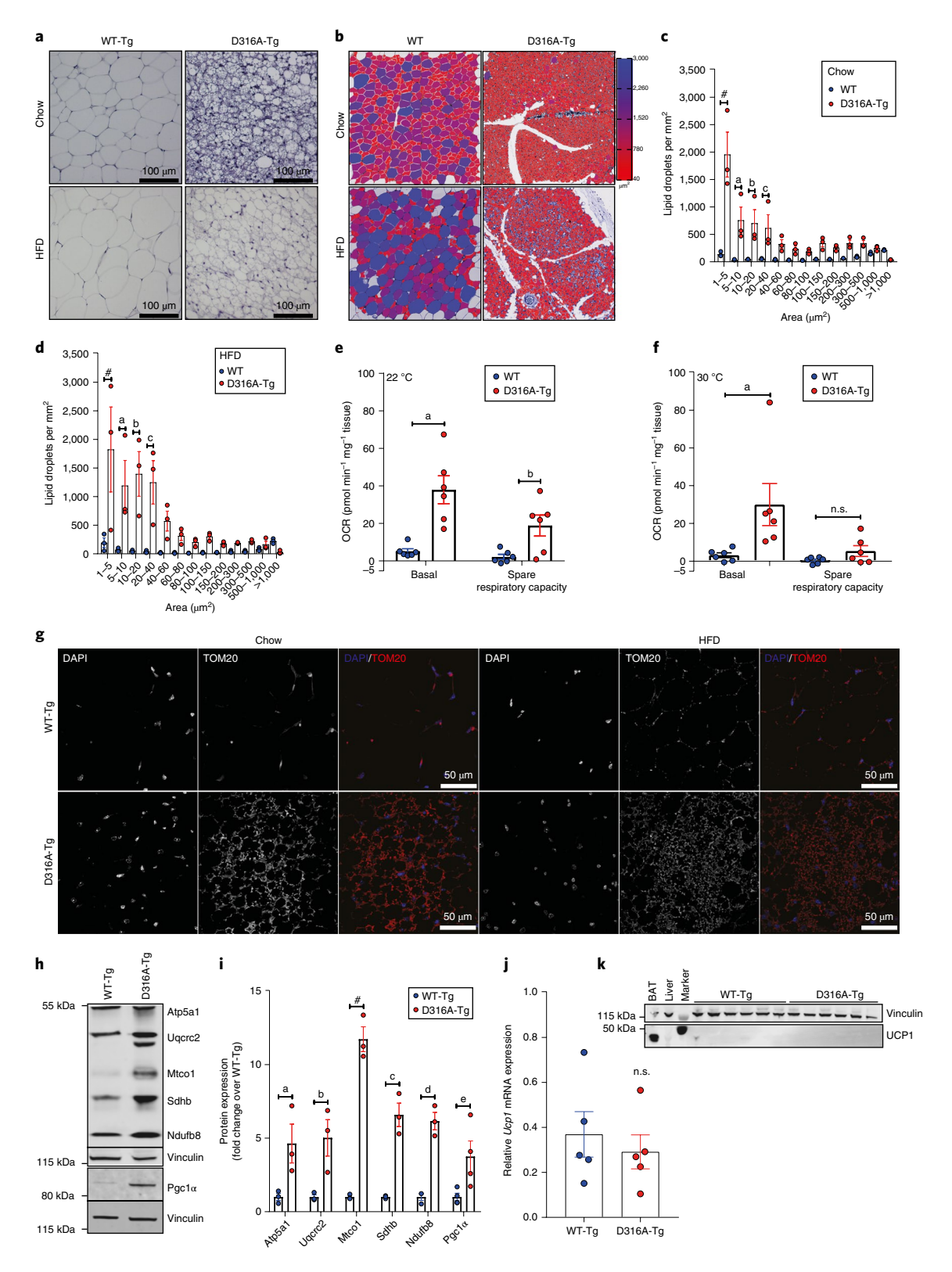
The studies described above use a gain-of-function AMPK model that is present from birth, which would not be a desirable therapeutic strategy. To better reflect a therapeutic approach, we used an inducible β-actin-Cre line (CAGGCre-ER) to determine the effect of AMPK activation following the onset of diet-induced obesity. Male mice 8 weeks of age were switched to a HFD, and 4 weeks later, transgene expression was induced by tamoxifen injection. Mice expressing either the floxed y1 allele or the CAGGCre-ER alone were injected with tamoxifen and used as controls (Control). Tamoxifen caused a drop in body weight in both control and D316A-Tg mice, but the D316A-Tg mice gained significantly less weight over the next 7 weeks on HFD (Supplementary Fig. 6). At that point, 7 weeks after administration of tamoxifen, the control mice had gained more than threefold the weight of the D316A-Tg mice $(5.6 \pm 1.3 \text{ versus } 1.8 \pm 1.4 \text{ g})$ (n = 9 per group), as compared with their body weight immediately before tamoxifen injection). This was reflected by a significantly lower total fat mass in the D316A-Tg mice (Supplementary Fig. 6). Immunohistochemical analysis revealed that adipocytes isolated from both BAT and WATsc of

Fig. 3 | AMPK activation increases subcutaneous white adipose mitochondrial content and Ucp1-independent respiration. a, Representative image (from six or seven mice per group from a single experimental cohort) of haematoxylin-stained sections of WATsc from mice maintained on chow or HFD for 4 weeks (scale bar, 100 μm). **b**, Examples of 1-mm² regions of interest (ROI) selected for quantification. Three regions per mouse were quantified, and this process was repeated for three mice per group. Lipid-droplet size is represented by the heat scale shown alongside. **c**, Quantification of lipid-droplet size on chow diet. ${}^{a}P = 0.001$, ${}^{b}P = 0.0038$, ${}^{c}P = 0.0212$, ${}^{a}P < 0.0001$. **d**, Quantification of lipid-droplet size on HFD. ${}^{a}P = 0.004$, ${}^{b}P = 0.0003$, ${}^{c}P = 0.0015$, ${}^{a}P < 0.0001$. **e**, Basal OCR and spare respiratory capacity measured in adipose tissue explants from wild-type (WT) and D316A-Tg mice (n = 6 per genotype) housed at 22 °C and fed a HFD for 8 weeks. ${}^{a}P = 0.0001$, ${}^{b}P = 0.0269$. **f**, OCR and spare respiratory capacity in adipose tissue explants from mice housed at 30 °C and fed a HFD for 11 weeks. ${}^{a}P = 0.00076$, n.s., not significant. **g**, Representative images (three images per section from six or seven mice per group from a single experimental cohort) of immunofluorescence staining of mitochondrial outer-membrane protein Tom-20 (denoted by red in the merged images), counterstained with DAPI to stain nuclei (shown in blue in the merged images) in WATsc (scale bar, 50 μm). Similar results were obtained from two independent cohorts. **h**, Representative immunoblot analysis of mitochondrial electron-transport-chain proteins and Pgc1α in WATsc from mice fed a HFD. **i**, Quantification of protein expression (n = 3 - 4 mice per genotype). ${}^{a}P = 0.0037$, ${}^{b}P = 0.0005$, ${}^{c}P = 0.0001$, ${}^{d}P = 0.0003$, ${}^{c}P = 0.0039$, ${}^{c}P = 0.0001$, ${}^{c}P$

D316A-Tg mice had smaller lipid droplets than those in control mice, and liver triglyceride content was markedly reduced in the D316A-Tg mice (Supplementary Fig. 6). In agreement with findings in the constitutive β -actin-cre model, immunoblotting showed that components of the mitochondrial electron-transport chain were increased in WATsc of D316A-Tg mice, and there were significant increases in Atp5a1 and Sdhb (Supplementary Fig. 6). Together, these results demonstrate that the effects of AMPK activation are

not developmental in origin, thus adding considerable strength to the translational potential of AMPK activation in protecting against diet-induced obesity.

One of the major pharmacological approaches to targeting obesity is activation of pathways that increase energy expenditure to reduce positive energy balance. Here we show that genetic activation of AMPK increases energy expenditure in mice fed a HFD, through Ucp1-independent thermogenesis in WATsc. Previous



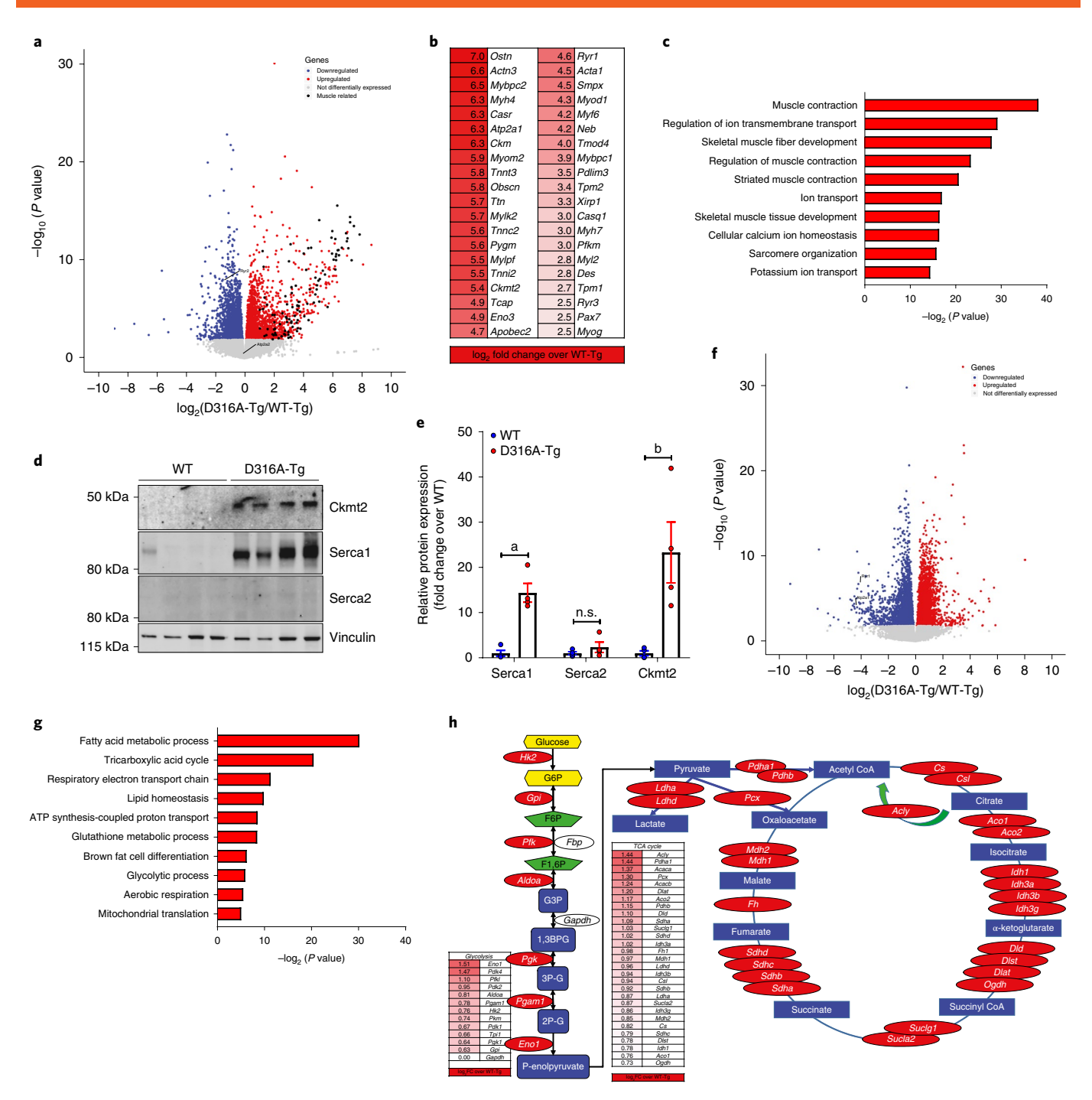


Fig. 4 | AMPK activation induces a skeletal muscle-like gene signature in WATsc in mice fed a HFD. **a**, RNA-sequencing analysis was used to determine changes in gene expression in WATsc isolated from WT-Tg and D316A-Tg mice fed a HFD for 16 weeks (n=6 mice per genotype). Volcano plot with downregulated genes shown in blue, upregulated genes in red and unchanged genes in gray. A total of 1,353 genes were upregulated and 1,102 downregulated (fold change > 1.5). Differentially expressed genes (DEGs) were identified (P < 0.05) by using DESeq2 (Wald test) in R. DEGs are expressed as \log_2 fold change over WT-Tg with an adjusted P value for each gene. Skeletal muscle-associated genes are shown in black. Cardiac isoforms of Serca (Atp2a2) and ryanodine receptor (Ryr2) are also highlighted. **b,c**, The 40 most highly upregulated skeletal muscle-associated genes (**b**) and the most significantly enriched gene ontology annotations (**c**) for the 100 most highly upregulated genes are shown. Associated P values were determined according to analysis in the Database for Annotation, Visualization, and Integrated Discovery (Fisher exact P value). **d,e**, Immunoblot (**d**) and quantification of Ckmt2, Serca1 and Serca2 (**e**) in WATsc isolated from mice fed a HFD for 16 weeks (n=4 per genotype from two independent experimental cohorts). Protein expression was normalized to that of vinculin, and expression is shown as fold change relative to wild type (WT). Significant differences from WT are shown as $^{a}P = 0.0026$ and $^{b}P = 0.0494$; n.s., not significant. **f**, Volcano plot as in **a** for WATsc from mice fed a chow diet (n=6 mice per genotype). In total, 1,361 genes were upregulated, and 1,808 were downregulated. Atp2a1 and Ryr1 are highlighted on the plot. **g**, The most significantly enriched gene ontology annotations for significantly upregulated genes are shown. **h**, A schematic diagram showing upregulated genes (highlighted in red) in glycolysis and the TCA cycle in D316A WATsc in mice fed a chow diet

studies using AMPK-deletion models have reported the effects of AMPK on UCP1-dependent thermogenesis in both BAT and WAT³⁰⁻³². Pharmacological activation of AMPK has been reported to increase BAT mass in the offspring of obese mice30 and to increase UCP1 expression in WAT31. In our study, UCP1 expression was not affected by AMPK activation in either global or adipose tissue-specific models. Together, these studies indicate that AMPK plays an important role in the development of both BAT and WAT. However, further studies are required to elucidate the precise role of AMPK activation in regulating the thermogenic programme in adipose tissue. Importantly, our findings strengthen the idea that AMPK activators have considerable potential in treating metabolic diseases, including obesity. In this study, we show that AMPK activation increases the population of a novel type of adipocyte within the subcutaneous white adipose depot; these adipocytes resemble brown adipocytes but lack Ucp1 expression. At present, the origin of these cells remains unknown, and further characterization of these cells is a major challenge for futre studies. Additionally, the mechanism leading to thermogenesis in these cells remains to be established. Nonetheless, induction of these precursor cells provides an exciting novel pharmacological target for exploiting as a therapeutic strategy in treating obesity.

Methods

Animals. All in vivo studies were performed in accordance with the United Kingdom Animals (Scientific Procedures) Act (1986) and were approved by the Animal Welfare and Ethical Review Board at Imperial College London. The Rosa26 gene targeting vector was prepared from a mouse C57BL/6 bacterial artificial chromosome with homology arms 5.6 kilobases and 1.7 kilobases flanking the XbaI site in the Rosa26 gene, and a sequence encoding the Flag epitope (DYKDDDDK) at the C terminus was engineered into the constructs to allow recognition by an anti-Flag antibody. Targeted ES cells were injected into BalbC/cANnCrl (Charles River) blastocysts, and embryos were implanted into pseudopregnant C57Bl6NCrl female mice. The resulting chimeric animals were mated with C57BL/6N mice to produce agouti heterozygous animals (F1). To generate animals without the Neo cassette, we bred F₁ mice with CAG-FlpO. These mice were crossed with mice expressing Cre-recombinase under the control of the β -actin promoter (Tmeme163^{Tg(ACTB-cre)2Mrt} (stock 003376; Jackson Laboratories) to generate mice with ubiquitous expression of the γ1 transgene (referred to as WT-Tg and D316A-Tg mice). Adipose-specific expression was achieved by crossing the γ1 floxed mice with mice expressing Cre-recombinase under the control of the adiponectin promoter (Adipoq-Cre; B6.FVB-Tg(Adipoq-cre)1Evdr/J; stock 028020; Jackson Laboratories) or the Pdgfrα promoter (C57BL/6-Tg(Pdgfra-cre)1Clc/J; stock 013148; Jackson Laboratories). Muscle-specific expression was achieved by crossing the $\gamma 1$ floxed mice with mice expressing Cre-recombinase under the control of the Mef2c promoter (C57BL/6-Tg(Mef2c-cre)2Blk: a generous gift from B. L. Black (University of California San Francisco)). For inducible expression, mice were crossed with mice expressing Cre-recombinase under the control of a tamoxifen-inducible chicken β-actin promoter (CAGGCre-ERTM; B6.Cg-Tg(CAG-cre/Esr1*)5Amc/J; stock 004682; Jackson Laboratories). Induction was achieved by intraperitoneal injection of mice with 3 mg tamoxifen in 0.15 ml corn oil (four daily injections). Unless stated otherwise, male mice were used for all studies and were maintained on a 12-h light/dark cycle at 22 °C with free access to food and water, and group-housed in specific-pathogen-free barrier facilities. Chow-standard breeding diet number 3 was obtained from Special Diets Services, and the HFD (45% energy from fat) was obtained from TestDiet. Unless otherwise stated, for HFD feeding, the diet was switched at 8 weeks of age. At the end of the procedure, animals were killed by cervical dislocation, and organs were harvested rapidly, weighed and either frozen in liquid nitrogen for further analysis or placed in 4% paraformal dehyde for subsequent histological analysis.

Metabolic phenotyping. The whole-animal oxygen consumption rate (VO₂) was measured by using a Columbus Instruments Comprehensive Laboratory Animal Monitoring System. Before these studies, mice were singly housed for 1 week to acclimate them to the housing conditions. Animals were fed ad libitum in all studies using this system. Animals were weighed before being placed in designated cages, with an even distribution of genotypes between each rack. VO₂ consumption was calculated by built-in software (Oxymax) and normalized to body weight. Movement was measured by counting horizontal beam breaks. Recordings were taken at regular intervals throughout the duration of the experiment. In some cases, mice were housed at 30 °C (within their thermoneutral zone). For the $\beta 3$ -agonist study, mice were removed from the cages and injected intraperitoneally with CL316, 243 (1 mg kg $^{-1}$) or vehicle control, then returned to their cages for monitoring of oxygen consumption. In some cases, VO $_2$ time series data were

smoothed by using a running average method, with GraphPad Prism software, and average VO2 values calculated. Food intake on chow was measured manually by recording the daily mass of diet used over a 3-week period. Food intake on the HFD was measured by using BioDAQ food intake monitoring cages (Research Diets, Inc.) and measuring the ad libitum feeding activity over a 5-d period. Mice were fed from gated hoppers mounted outside of the cage to reduce variability. Data were recorded by using the BioDAQ DataViewer. Total body composition was measured by using an EchoMRI body composition analyser. Core body temperature was measured by using a rectal thermal probe, and subcutaneous temperature was measured by using IPTT300 BMDS transponders inserted subcutaneously into the left or right flank. Liver triglyceride content was measured by using Triglyceride liquid (Sentinel Diagnostics). Glucose tolerance tests were performed on mice after a 6-h overnight fast. Animals were given an oral bolus of glucose (2 g kg-1 lean body mass), and blood glucose levels were determined by a glucometer at the indicated time points. Serum insulin was measured in mice either fasted for 6h or fasted/re-fed for 2h, by using an Ultra-Sensitive Mouse Insulin ELISA kit (CrystalChem). Electrocardiographs from conscious, unrestrained mice were recorded by using the ECGenie System (Mouse Specifics, Inc.).

Treatment with β-guanidinopropionic acid. In some cases, mice were transferred to a HFD and after 1 week were given access to water containing 0.5% β-guanidinopropionic acid and 0.13% saccharin, or water containing only 0.13% saccharin. Water, food intake and body weight were monitored over the next 3 weeks.

Measurement of respiration in white adipose tissue explants. Subcutaneous white adipose tissue (1.5–2.0 mg) was obtained by using a Biopsy Puncher (2 mm), placed into XF24 Islet Capture Microplates and incubated in assay medium (substrate-free DMEM (Sigma, D5030), 30 mM sodium chloride, pH 7.4, 25 mM glucose, 0.5 mM sodium pyruvate). Oxygen consumption rate was measured on a Seahorse XF24 Flux analyser after sequential addition of oligomycin (5 μ M), carbonyl cyanide 3-chlorophenyl hydrazone (5 μ M) and antimycin (5 μ M).

Histological analysis. Tissues were fixed in 4% paraformaldehyde overnight and dehydrated by incubation in 50% and then 70% ethanol. Samples were wax embedded in paraffin and sectioned to a thickness of 4 µm. Tissues were deparaffinized and rehydrated with Acquaclear, 100% and then 70% ethanol, and boiled in sodium citrate antigen retrieval solution for 5 min in a pressure cooker. Sections were stained with haematoxylin and eosin, or with an anti-glycogen phosphorylase antibody on a Discovery Ultra (Ventana Medical Systems). The secondary antibody used was Discovery OmniMap anti-rabbit HRP (RUO), which was detected with the ChromoMap DAB Kit (RUO). Stained sections were visualized under bright-field microscopy. For immunofluorescence staining, slides were washed in Tris-buffered saline (TBS) and blocked by incubation with 0.2% (w/v) fish-skin gelatin for 1 h at room temperature. Sections were then incubated with primary antibody in 0.2% fish-skin gelatin overnight at 4°C. Slides were washed in 10 mM Tris-HCl, pH 7.4, and 150 mM sodium chloride containing 0.1% Tween-20 and incubated with an Alexa Fluor-conjugated secondary antibody (488 green or 633 red) for 1 h at room temperature. After subsequent washes with TBS, sections were incubated with DAPI to stain nuclei for 5 min, rinsed under running water and mounted by using VectaShield immunofluorescence mounting medium. Immunofluorescence-stained sections were imaged by using a Leica TCS SP5 confocal microscope at 200 Hz, with either a Leica ×20/0.7 numerical aperture (NA) Plan-Apochromat (PL-APO), ×40/1.25-NA PL-APO or ×63/1.4-NA PL-APO objective lens, and analysed by using LASAF software (Leica). A custom ImageJ macro script was developed to automate lipid-droplet identification and area quantification from 1-mm2 regions of interest. Briefly, images of tissue sections were acquired on a Zeiss AxioScan.Z1 digital slide scanner with a ×20/0.8-NA PL-APO objective lens. Images were converted to grayscale and filtered to enhance the stained boundaries. Images were then thresholded and binarized for detection of lipid-droplet boundaries, the resultant binary mask was inverted, and a watershed operation was applied to segment individual adipocytes. Further refinement of individual adipocyte and lipid-droplet identification was achieved by filtering on the basis of morphological measurements, specifically circularity and aspect ratio, in addition to manual editing.

Immunoblot analysis. Tissues were homogenized by using an Ultra-Turrax homogenizer in $10\times$ (w/v) ice-cold homogenization buffer containing 50 mM Tris, 50 mM sodium fluoride, 5 mM napyrophosphate, 1 mM ethylenediaminetetraacetic acid, 0.25 M mannitol, 1 mM dithiothreitol, 157 µg ml $^{-1}$ benzamidine, 4 µg ml $^{-1}$ trypsin inhibitor and 0.1 mM phenylmethylsulfonyl fluoride. Homogenates were centrifuged at 13,000g for 15 min to remove insoluble material. Protein content of the soluble fraction was quantified by using a BCA assay kit (ThermoScientific). Proteins (50 µg total) were resolved by SDS–PAGE and transferred to a polyvinylidene difluoride membrane (Millipore Immobilon-FL) at 100 V for 90 min. Membranes were stained with PonceauS to check protein transfer and blocked in 4% (w/v) bovine serum albumin for 1 h at room temperature. Unless stated otherwise, primary antibodies were diluted 1:1,000 in TBS containing 4% bovine serum albumin and 0.1% Tween-20, and incubated with the membrane for

 $4\,h$ at room temperature or overnight at $4\,^{\circ}\text{C}$. Membranes were washed extensively with TBS containing 0.1% Tween-20 before incubation with an appropriate IRDye secondary antibody (LI-COR Biosciences) in TBS for $1\,h$ at room temperature. Blots were visualized with an Odyssey Imaging System (LI-COR Biosciences) and quantified by using ImageStudio 4.0.

Antibodies. The following antibodies were used in this study: total OXPHOS antibody cocktail (Abcam, ab110413); Ckmt2 (Abcam, ab55963); anti-Flag (Cell Signalling, 14793); anti-Pgc1-α (Abcam, ab54481); anti-Tom-20 (SantaCruz, sc-11415); anti-Serca1 (Abcam, ab109899); anti-Serca2 (Invitrogen, MA3-919); anti-Ucp1 (Abcam, ab 10983); and anti-vinculin (Sigma, V9131).

RNA isolation. Total RNA was isolated from snap-frozen tissue by homogenization in 1 ml TRIzol (Life Technologies) per 100 mg tissue on ice. Samples were stored overnight at $-20\,^{\circ}\mathrm{C}$ and centrifuged at 10,000g for 15 min, and the homogenate was removed to a fresh tube. Chloroform (400 ml ml $^{-1}$) was added, and the mixture centrifuged at 10,000g for 15 min at room temperature. The aqueous phase was transferred to an RNase-free microcentrifuge tube, and absolute ethanol (0.53× volume) added. RNA was purified with RNeasy Mini spin columns (Qiagen). RNA was eluted in 50 μ l RNase-free water and quantified by using a NanoDrop spectrophotometer. Samples were frozen at $-80\,^{\circ}\mathrm{C}$ until required.

Quantitative reverse-transcription polymerase chain reaction. RNA (3 µg) was incubated with $1\,\mu l$ random hexamers (50 ng μl^{-1}), $1\,\mu l$ 10 mM deoxynucleotide triphosphated mix and diethyl pyrocarbonate water to 10 µl. Samples were incubated at 65 °C for 5 min on a thermal cycler. Next, 10 µl complementary DNA synthesis mix (containing 2 µl 10× RT buffer, 4 µl 25 mM MgCl₂, 2 µl 0.1 M dithiothreitol, 1 µl RNaseOut and 1 µl Superscript II (Qiagen)) was added to each sample and cycled as follows: 25 °C (10 min), 85 °C (50 min); the tubes were then transferred onto ice and allowed to cool. One microliter of RNase H was added to each sample and incubated at 37 °C for 10 min. To determine primer linearity, 5 μl cDNA from each sample was pooled and serially diluted to yield a standard curve. For each polymerase chain reaction, 5 µl cDNA was added to 10 µl 2× SYBR-HiROX (Bioline), 1.6 µl forward (AGCCATCTGCATGGGATCAAA) and reverse (GGGTCGTCCCTTTCCAAAGTG) primer mix and double-distilled water to a total reaction volume of 20 µl. The quantitative polymerase chain reaction plate was analysed by using an Opticon thermal cycler with Opticon monitor software to generate C, values for each reaction.

To quantify gene expression, C_i -value replicates were checked for primer efficacy (%) and consistency. Average C_i values were then calculated for each sample, and quantified by using a linear equation (y = mx + c) previously determined from the standard curve corresponding to the gene of interest. The equation was solved for x, with y as C_i value. This value was then transformed by using 10^x , as the standard curve was generated on a logarithmic scale. This process was repeated for all genes, including a designated housekeeping gene. Unless otherwise stated, all experiments were normalized to Polr2a, an RNA polymerase that has been shown to remain stable across dietary interventions.

Gene expression was then presented as both a ratio to the expression of the housekeeping gene for the experiment, and as fold change over the designated control.

RNA-sequencing analysis. RNA was extracted from subcutaneous white adipose (six mice per genotype fed either chow or a HFD for 16 weeks, processed individually). For each sample, 2 µg RNA in 60 µl RNase-free water was quality assessed by using a BioAnalyzer RNA kit (Agilent). An RNA-integrity-number score >7 was required for further analysis. The RNA libraries were prepared by using a TruSeq Stranded mRNA Library Prep Kit (Illumina) and standard Illumina protocol. Libraries were quantified with a Qubit HS (ThermoFisher) and Agilent BioAnalyzer adjusted to the appropriate concentration for sequencing. Indexed libraries were pooled and sequenced at a final concentration of 1.6 pM on an Illumina NextSeq 500 high-output run by using paired-end chemistry with 75-base pair read length. The sequencing data were demultiplexed by using Illumina bcl2fastq2-v2.16. The quality of the reads was assessed by using FastQC (https://www.bioinformatics.babraham.ac.uk/projects/fastqc/). The reads were processed and mapped to the mouse genome mm10 by using Bcbio-nextgen framework v.0.9.0 (https://github.com/chapmanb/bcbio-nextgen). The aligner used was STAR 2.4.1d, and alignment quality was assessed with QualiMap v.2.1.1.

Identification of differentially expressed genes was performed by using DESeq2 in R. A principal component analysis was generated as a quality-control step, to assess the clustering of samples in terms of gene expression. A list of differentially expressed genes was generated, expressed as \log_2 fold change over the control sample (WT-Tg), with an adjusted P value for each gene.

Analysis of differentially expressed genes. Using original DESeq2 output Excel files, we listed genes in order of \log_2 fold change with an adjusted P threshold of 0.05 and a biological threshold of ± 1.5 -fold change relative to WT-Tg. Ingenuity Pathway Analysis (Qiagen Bioinformatics) was used to analyse the lists of differentially expressed genes defined according to P < 0.05. Gene ontology enrichment analysis was performed by using the Database for Annotation,

Visualization, and Integrated Discovery to find gene ontology terms and Kyoto Encyclopaedia of Genes and Genomes pathways enriched within differentially expressed genes. For the HFD analysis, an input list consisting of the top 100 most upregulated genes (by fold change) was used. The Gene Expression Omnibus accession number for the RNA-sequencing data is GSE120429.

Statistical analysis. Unless stated otherwise, data presented are shown of mean \pm s.e.m. Graphpad Prism software (v.7) was used for graphing and statistical analysis. For comparison between two groups, datasets were analysed by Student's *t*-test with statistical significance defined as P < 0.05. To compare three or more datasets, one-way ANOVA was used, followed by Bonferroni's range test to measure significance between means. Multiple comparisons were analysed by two-way ANOVA, followed by Bonferroni's multiple-comparisons test to determine the statistical significance between groups on the basis of one variable. For RNA-sequencing analyses, an adjusted P value threshold was determined at 0.05.

Reporting Summary. Further information on research design is available in the Nature Research Reporting Summary linked to this article.

Data availability

The datasets that support the findings of this study are available from the corresponding author upon request. RNA-sequence datasets used in this study are available from Gene Expression Omnibus with the accession number GSE120429.

Received: 29 May 2018; Accepted: 17 January 2019; Published online: 25 February 2019

References

- Carling, D. AMPK signalling in health and disease. Curr. Opin. Cell Biol. 45, 31–37 (2017).
- Hardie, D. G. AMP-activated protein kinase: maintaining energy homeostasis at the cellular and whole-body levels. Annu. Rev. Nutr. 34, 31–55 (2014).
- Steinberg, G. R. & Kemp, B. E. AMPK in health and disease. *Physiol. Rev.* 89, 1025–1078 (2009).
- Cool, B. et al. Identification and characterization of a small molecule AMPK activator that treats key components of type 2 diabetes and the metabolic syndrome. *Cell Metab.* 3, 403–416 (2006).
- Xiao, B. et al. Structural basis of AMPK regulation by small molecule activators. Nat. Commun. 4, 3017 (2013).
- Woods, A. et al. Liver-specific activation of AMPK prevents steatosis on a high fructose diet. Cell Rep. 18, 3043–3051 (2017).
- Andersson, U. et al. AMP-activated protein kinase plays a role in the control of food intake. J. Biol. Chem. 279, 12005–12008 (2004).
- Minokoshi, Y. et al. AMP-kinase regulates food intake by responding to hormonal and nutrient signals in the hypothalamus. *Nature* 428, 569–574 (2004).
- Nicholls, D. G. & Locke, R. M. Thermogenic mechanisms in brown fat. Physiol. Rev. 64, 1–64 (1984).
- Cannon, B. & Nedergaard, J. Brown adipose tissue: function and physiological significance. *Physiol. Rev.* 84, 277–359 (2004).
- Feldmann, H. M., Golozoubova, V., Cannon, B. & Nedergaard, J. UCP1 ablation induces obesity and abolishes diet-induced thermogenesis in mice exempt from thermal stress by living at thermoneutrality. *Cell. Metab.* 9, 203–209 (2009).
- García-Ruiz, E. et al. The intake of high-fat diets induces the acquisition of brown adipocyte gene expression features in white adipose tissue. *Int. J. Obes.* 39, 1619–1629 (2015).
- Gordon, C. J. Thermal physiology of laboratory mice: defining thermoneutrality. J. Therm. Biol. 37, 654–685 (2012).
- Walden, T. B., Hansen, I. R., Timmons, J. A., Cannon, B. & Nedergaard, J. Recruited vs. nonrecruited molecular signatures of brown, "brite," and white adipose tissues. Am. J. Physiol. Endocrinol. Metab. 302, E19–E31 (2012).
- 15. Wu, J., Cohen, P. & Spiegelman, B. M. Adaptive thermogenesis in adipocytes: is beige the new brown? *Genes Dev.* 27, 234–250 (2013).
- Harms, M. & Seale, P. Brown and beige fat: development, function and therapeurtic potential. Nat. Med. 19, 1252–1263 (2013).
- 17. Wu, J. et al. Beige adipocytes are a distinct type of thermogenic fat cell in mouse and human. *Cell* **150**, 366–376 (2012).
- Granneman, J. G., Burnazi, M., Zhu, Z. & Schwamb, L. A. White adipose tissue contributes to UCP1-independent thermogenesis. Am. J. Physiol. Endocrinol. Metab. 285, E1230–E1236 (2003).
- Ukropec, J., Anunciado, R. P., Ravussin, Y., Hulver, M. W. & Kozak, L. P. UCP1-independent thermogenesis in white adipose tissue of cold-acclimated Ucp1-fr mice. J. Biol. Chem. 281, 31894–31908 (2006).
- Kazak, L. et al. A creatine-driven substrate cycle enhances energy expenditure and thermogenesis in beige fat. Cell 163, 643–655 (2015).
- Fitch, C. D. & Chevli, R. Inhibition of creatine and phosphocreatine accumulation in skeletal muscle and heart. *Metabolism* 29, 686–690 (1980).

- Block, B. A., O'Brien, J. & Meissner, G. Characterization of the sarcoplasmic reticulum proteins in the thermogenic muscles of fish. J. Cell. Biol. 127, 1275–1287 (1994).
- 23. da Costa, D. C. & Landeira-Fernandez, A. M. Thermogenic activity of the Ca²⁺-ATPase from blue marlin heater organ: regulation by KCl and temperature. *Am. J. Physiol. Regul. Integr. Comp. Physiol.* **297**, R1460–R1468 (2009).
- 24. Ikeda, K. et al. UCP1-independent signaling involving SERCA2b-mediated calcium cycling regulates beige fat thermogenesis and systemic glucose homeostasis. *Nat. Med.* 23, 1454–1465 (2017).
- Inagaki, T., Sakai, J. & Kajimura, S. Transcriptional and epigenetic control of brown and beige adipose cell fate and function. *Nat. Rev. Mol. Cell Biol.* 17, 480–495 (2106).
- Sanchez-Gurmaches, J., Hung, C. M. & Guertin, D. A. Emerging complexities in adipocyte origins andidentity. *Trends Cell Biol.* 26, 313–326 (2016).
- Eguchi, J. et al. Transcriptional control of adipose lipid handling by IRF4. Cell. Metab. 13, 249–259 (2011).
- 28. Jeffery, E. et al. Characterization of Cre recombinase models for the study of adipose tissue. *Adipocyte* 3, 206–211 (2014).
- Berry, R. & Rodeheffer, M. S. Characterization of the adipocyte cellular lineage in vivo. *Nat. Cell Biol.* 15, 302–308 (2013).
- Yang, Q. et al. AMPK/α-ketoglutarate axis dynamically mediates DNA demethylation in the Prdm16 promoter and brown adipogenesis. *Cell Metab.* 24, 542–554 (2016).
- 31. Wu, L. et al. AMP-activated protein kinase (AMPK) regulates energy metabolism through modulating thermogenesis in adipose tissue. *Front. Physiol.* **9**, 122 (2018).
- Mottillo, E. P. et al. Lack of adipocyte AMPK exacerbates insulin resistance and hepatic steatosis through brown and beige adipose tissue function. *Cell Metab.* 24, 118–129 (2016).

Acknowledgements

This work was funded by the Medical Research Council UK (grant MC-A654-5QB10 to D.C.). A.E.P. was funded by a BBSRC-CASE Studentship Award (BB/L502662/1). L.W. was funded by a British Heart Foundation Studentship Award. We would like to thank the MRC London Institute of Medical Sciences Whole Animal Physiology Team for their assistance.

Author contributions

A.E.P., L.M., P.J.M., T.A., M.B., L.W. and R.F. carried out the in vivo and in vitro studies. S.K., A.B. and M.C. carried out the RNA sequencing and analysis. C.W. and D.S. helped with immunohistochemistry analysis. A.S. and M.B.Y. helped with the metabolic phenotyping. L.P. and A.W. helped perform phenotypic analysis of mice. A.E.P., L.M., W.K. and M.R.D. carried out the cellular respiration studies. A.E.P., L.M., A.W., D.M.S., J.A.R., M.A.S. and D.C. designed and planned the study. All authors contributed to the preparation of the manuscript.

Competing interests

The authors declare no competing interests.

Additional information

Supplementary information is available for this paper at https://doi.org/10.1038/ \pm 2255-019-0036-9.

Reprints and permissions information is available at www.nature.com/reprints.

Correspondence and requests for materials should be addressed to A.W. or D.C.

Publisher's note: Springer Nature remains neutral with regard to jurisdictional claims in published maps and institutional affiliations.

© The Author(s), under exclusive licence to Springer Nature Limited 2019



|--|

Reporting Summary

Nature Research wishes to improve the reproducibility of the work that we publish. This form provides structure for consistency and transparency in reporting. For further information on Nature Research policies, see <u>Authors & Referees</u> and the <u>Editorial Policy Checklist</u>.

When statistical analyses are reported, confirm that the following items are present in the relevant location (e.g. figure legend, table legend, main

Statistical parameters

text,	or I	Methods section).
n/a	Cor	nfirmed
	\boxtimes	The $\underline{\text{exact sample size}}(n)$ for each experimental group/condition, given as a discrete number and unit of measurement
	\boxtimes	An indication of whether measurements were taken from distinct samples or whether the same sample was measured repeatedly
	\boxtimes	The statistical test(s) used AND whether they are one- or two-sided Only common tests should be described solely by name; describe more complex techniques in the Methods section.
	\boxtimes	A description of all covariates tested
	\boxtimes	A description of any assumptions or corrections, such as tests of normality and adjustment for multiple comparisons
	\boxtimes	A full description of the statistics including <u>central tendency</u> (e.g. means) or other basic estimates (e.g. regression coefficient) AND <u>variation</u> (e.g. standard deviation) or associated <u>estimates of uncertainty</u> (e.g. confidence intervals)
	\boxtimes	For null hypothesis testing, the test statistic (e.g. <i>F</i> , <i>t</i> , <i>r</i>) with confidence intervals, effect sizes, degrees of freedom and <i>P</i> value noted <i>Give P values as exact values whenever suitable.</i>
\boxtimes		For Bayesian analysis, information on the choice of priors and Markov chain Monte Carlo settings
\boxtimes		For hierarchical and complex designs, identification of the appropriate level for tests and full reporting of outcomes
\boxtimes		Estimates of effect sizes (e.g. Cohen's d , Pearson's r), indicating how they were calculated
		Clearly defined error bars

Our web collection on <u>statistics for biologists</u> may be useful.

Software and code

Policy information about availability of computer code

State explicitly what error bars represent (e.g. SD, SE, CI)

Data collection

For RNA sequencing, reads were processed and mapped to the mouse genome mm10 using the Bcbio-nextgen framework version 0.9.0. The aligner used was STAR 2.14.1d and alignment quality assessed with QualiMap v.2.1.1. Differentially expressed genes were identified using DESeq2.1.1.

Data analysis

Ingenuity Pathway Analysis (Qiagen Bioinformatics) was used to analyse differentially expressed genes. Gene ontology (GO) enrichment analysis was performed using the Database for Annotation, Visualization, and Integrated Discovery (DAVID) to find Gene Ontology (GO) terms and Kyoto Encyclopedia of Genes and Genomes (KEGG) pathways enriched within differentially expressed genes.

Microsoft Excel v15.25 for Mac and GraphPad Prism v7 were used for all other data analysis. For oxygen consumption in mice, Oxymax v4.4 (Columbus Instruments) was used for data analysis. Opticon Monitor v3.1 was used for analysis of RT-PCR data. LAS AF v. 2.7.3.9723 software was used for SP5 confocal microscopy. R v3.2.0 was used for DSeq2 normalisation of RNA sequencing data.

For manuscripts utilizing custom algorithms or software that are central to the research but not yet described in published literature, software must be made available to editors/reviewers upon request. We strongly encourage code deposition in a community repository (e.g. GitHub). See the Nature Research guidelines for submitting code & software for further information.

Data

Policy information about availability of data

All manuscripts must include a <u>data availability statement</u>. This statement should provide the following information, where applicable:

- Accession codes, unique identifiers, or web links for publicly available datasets
- A list of figures that have associated raw data
- A description of any restrictions on data availability

available from the corresponding author on reasonable request.						
Field-spe	ecific reporting					
Please select the b	ease select the best fit for your research. If you are not sure, read the appropriate sections before making your selection.					
Life sciences	Behavioural & social sciences Ecological, evolutionary & environmental sciences					
For a reference copy of	the document with all sections, see <u>nature.com/authors/policies/ReportingSummary-flat.pdf</u>					
Life scier	nces study design					
All studies must dis	sclose on these points even when the disclosure is negative.					
Sample size	For in vivo studies, in most cases a minimum of 6 mice per condition was used. Based on our own previous experience, as well as results from other similar published studies, this sample size provides sufficient power to detect physiologically relevant changes. No Power calculations were performed for ex vivo studies (e.g. western blotting, RT-PCR). Sample size was between 3-6 independent samples and was based on availability of samples.					
Data exclusions	In one case, a mouse was excluded from the in vivo oxygen consumption determination because the readings were abnormally low. The reason for this was later identified as an error with the flow rate/oxygen calibration system for that specific cage unit. This error was not predetermined.					
Replication	In vivo experiments were carried out on multiple independent cohorts of animals with similar results. Oxygen consumption in adipose tissue measured ex vivo was performed on tissue from individual mice and repeated on different days, yielding similar results (significant differences between wild type and gain-of-function AMPK mice).					
Randomization	Mice were not randomized, but experiments were performed on cohorts of age and sex matched mice with the appropriate genotype.					
Blinding	Investigators were not blinded during the in vivo studies (in most cases, the bodyweight difference between genotypes is obvious).					

Reporting for specific materials, systems and methods

Materials & experimental systems			Methods	
n/a	Involved in the study	n/a	Involved in the study	
	Unique biological materials	\boxtimes	ChIP-seq	
	Antibodies	X	Flow cytometry	
	Eukaryotic cell lines	\boxtimes	MRI-based neuroimaging	
\boxtimes	Palaeontology			
	Animals and other organisms			
\boxtimes	Human research participants			

Unique biological materials

Policy information about <u>availability of materials</u>

Obtaining unique materials Unique materials are available upon request, and following completion of a material transfer agreement.

Antibodies

Antibodies used

All antibodies were used according to the supplier's instructions.

Vinculin (Sigma V9131), 1:1000 dilution; PGC1a (Abcam ab54481), 1:1000; Total OXPHOS monoclonal cocktail (Abcam ab110413), 1:1000; UCP1 (Abcam ab10983), 1:1000; Atp2a1 (Abcam ab109899), 1:1000; Atp2a2 (Invitrogen MA3-919), 1:1000; Ckmt2 (abcam ab55963), 1:1000; FLAG (Cell Signaling, 14793), 1:1000; TOM-20 (SantaCruz, sc-11415), 1:200.

Validation

Vinculin: The antibody reacts with the 116 kDa vinculin band in immunoblotting. The product reacts with vinculin of many species. Good reactivity is obtained with human, bovine, chicken, dog, rat, mouse, turkey, and Xenopus. The antibody shows cross reactivity with smooth muscle metavinculin. Citeab lists 635 citations.

PGC1a: Raised to synthetic peptide corresponding to Human PGC1 alpha aa 777-797. Validated for western blotting using mouse BAT. Referenced 150 times on Abcam website.

Total OXPHOS: The monoclonal antibodies in the cocktail were chosen because they are against a subunit that is labile when its complex is not assembled. Moreover, the combination is readily resolved in SDS-PAGE when the appropriate gel conditions are used. Referenced 279 times on Abcam website.

UCP1: Raised to synthetic peptide corresponding to Human UCP1 aa 145-159 conjugated to keyhole limpet haemocyanin. Validated for western blotting using rat BAT. Referenced 246 times on Abcam website.

Atp2a1: Raised against partial sequence of human Atp2a1 (amino acids 522-612). Antibody reactive against recombinant protein No longer available from Abcam, but now available from Novus Biologicals (H00000487-M01). No references available due to change in supplier/catalogue reference.

Atp2a2: MA3-919 has been successfully used in Western blot, immunocytochemistry and immunoprecipitation procedures. By Western blot, this antibody detects an ~110 kDa protein representing SERCA2 ATPase in rat cardiac tissue. Referenced 173 times on Sigma website.

Ckmt2: Raised against synthetic peptide corresponding to N terminal amino acids 37-86 of Human CKMT2. Positive control: Jurkat cell lysate Human skeletal muscle tissue. Referenced 3 times on Abcam website.

FLAG: Monoclonal antibody produced by immunizing animals with a synthetic DYKDDDIX peptide. Recognises FLAG epitope fused to either the amino-terminus or carboxy-terminus of the target protein. Referenced 48 times on Cell Signaling website. TOM-20: Detection of Tom20 of mouse, rat, human and avian origin by WB, IP, IF and IHC(P); also reactive with additional species, including and equine, canine, bovine, porcine and avian. This clone has been discontinued. Referenced 80 times on Santa Cruz website.

Eukaryotic cell lines

Policy information about cell lines

Cell line source(s)

 $\ensuremath{\mathsf{HEK293}}$ cells were obtained from the American Type Tissue Collection.

Authentication

HEK293 cells were not authenticated.

Mycoplasma contamination

HEK293 cells were tested using MycoAlert and cells tested were negative.

Commonly misidentified lines (See ICLAC register)

None were used in this study.

Animals and other organisms

Policy information about studies involving animals; ARRIVE guidelines recommended for reporting animal research

Laboratory animals

C57BL/6J mice harbouring either wild type AMPK gamma1 transgene (in the ROSA26 locus) or AMPK gamma1 with mutation of aspartic acid residue 316 to alanine, were used in this study. These mice were crossed with mice expressing cre-recombinase under the control of specific promoters, as described in the study. Male and female mice, aged between 8 - 30 weeks were used for studies.

Wild animals

No wild animals were used in the study.

Field-collected samples

No field-collected samples were used in the study.